Title

Competition between excitonic insulators and quantum Hall states in correlated electron—hole bilayers

Journal

Nature Materials

ISSN

1476-1122

Authors

Qi, Ruishi

Li, Qize

Zhang, Zuocheng

et al.

Publication Date

2025-08-25

DOI

10.1038/s41563-025-02316-5

Competition between excitonic insulators and quantum Hall states in correlated electron-hole bilayers

Ruishi Qi[1,2†], Qize Li[1,3†], Zuocheng Zhang[1], Jiahui Nie[1,3], Bo Zou[4], Zhiyuan Cui[1], Haleem Kim[1,2], Collin Sanborn[1,2,3], Sudi Chen[1], Jingxu Xie[1,2,3], Takashi Taniguchi[5], Kenji Watanabe[6], Michael F. Crommie[1,2], Allan H. MacDonald[4], Feng Wang[1,2,7,*]

[1] Department of Physics, University of California, Berkeley, CA 94720, USA.

[2] Materials Sciences Division, Lawrence Berkeley National Laboratory, Berkeley, CA 94720, USA.

[3] Graduate Group in Applied Science and Technology, University of California, Berkeley, CA 94720, USA.

[4] Department of Physics, University of Texas at Austin, Austin, TX 78712, USA.

[5] Research Center for Materials Nanoarchitectonics, National Institute for Materials Science, 1-1 Namiki, Tsukuba 305-0044, Japan.

[6] Research Center for Electronic and Optical Materials, National Institute for Materials Science, 1-1 Namiki, Tsukuba 305-0044, Japan.

[7] Kavli Energy NanoScience Institute, University of California Berkeley and Lawrence Berkeley National Laboratory, Berkeley, CA 94720, USA.

[†] These authors contributed equally to this work.

* To whom correspondence should be addressed: fengwang76@berkeley.edu.

Excitonic insulators represent a unique quantum phase of matter that enables the study of exotic quantum bosonic states. Strongly coupled electron-hole bilayers, which host stable dipolar exciton fluids with an exciton density that can be adjusted electrostatically, offer an ideal platform to investigate correlated excitonic insulators. Based on electron-hole bilayers made of $MoSe_2$/hBN/WSe_2 heterostructures, here we study the behavior of excitonic insulators in a perpendicular magnetic field. We report the observation of excitonic quantum oscillations in both Coulomb drag signals and electrical resistance at low to medium magnetic fields. Under a strong magnetic field, we identify multiple quantum phase transitions between the excitonic insulator phase and the bilayer quantum Hall insulator phase. These findings underscore the interplay between the electron-hole interactions and Landau level quantization, and enable further exploration of quantum phenomena in composite bosonic insulators.

Electron-hole (e-h) bilayers, where a two-dimensional electron gas (2DEG) and a 2D hole gas (2DHG) are confined to two closely spaced but electrically isolated layers[1–4], provide a versatile platform for studying quantum phases of correlated e-h fluids. Strong e-h Coulomb interactions lead to bound exciton states, while spatial separation suppresses recombination, enabling long-lived excitons in thermal equilibrium controllable by electrostatic gating. These systems are of great interest for exploring quantum bosonic and fermionic phases, including excitonic insulators (EIs)[1,3,4], Bose-Einstein condensates[2,5–9], and higher-order complexes such as trions and biexcitons[10–13].

Recent advances have enabled the creation of strongly coupled e-h bilayers using transition metal dichalcogenide (TMD) heterostructures[3,4,12–15]. With large effective mass and reduced dielectric screening in TMD systems, the strong Coulomb attraction across the layers leads to spontaneous formation of interlayer excitons. Compared with earlier system based on III-V semiconductor quantum wells or graphene[7,16–23], strong e-h coupling regime is accessible without external magnetic fields. A well-defined EI ground state at zero magnetic field has been reported, characterized by robust exciton binding, a large charge gap (~20 meV)[3,4] and perfect Coulomb drag[14,15]. Theoretical studies suggest that applying an out-of-plane magnetic field to such EIs induces quantum oscillations (QOs) via interplay between Coulomb interactions and magnetic cyclotron energy[24,25]. In the strong field limit, it is also predicted that the magnetic field can periodically destroy exciton binding and turn the EI into two independent quantum Hall insulators (QHIs)[24]. The appearance of QOs – a defining feature of a metallic system – in correlated insulating phases is intriguing, and has been a topic under decade-long debate[26–40]. Experimental evidence for the predicted excitonic QOs and quantum phase transitions have remained elusive.

In this paper, we report an experimental study of excitonic insulating e-h bilayers under an out-of-plane magnetic field in $MoSe_2$/hBN/WSe_2 heterostructures. At zero magnetic field, the EI phase is strongly insulating and exhibits perfect Coulomb drag behavior. As a magnetic field is applied, we observe clear QOs of drag currents and electrical resistances. At higher magnetic fields, we further observe multiple EI-QHI phase transitions.

Excitonic insulating electron-hole bilayers

Here we fabricate strongly coupled e-h bilayer devices based on $MoSe_2$/hBN/WSe_2 heterostructures, as illustrated in Fig. 1a. The device consists of two TMD monolayers – $MoSe_2$ (electron layer) and WSe_2 (hole layer) – separated by an ultrathin hBN tunneling barrier. They are sandwiched by graphite top gate (TG) and bottom gate (BG) with hBN dielectrics. Dual gates and separate TMD contacts allow independent electrostatic control of electron and hole densities. The $MoSe_2$ conduction band and WSe_2 valence band form a type-II band gap of ~1.5 eV. This charge gap can be electrically closed by a combination of interlayer bias voltage $V_{\mathrm{B}} \equiv V_h - V_e$ and vertical electric field $V_{\mathrm{BG}} - V_{\mathrm{TG}}$. We apply a large and fixed electric field, and continuously tune the charge gap with V_{B}. The symmetric gate voltage $V_{\mathrm{G}} \equiv V_{\mathrm{TG}}/2 + V_{\mathrm{BG}}/2$ sets the Fermi level and controls the e-h density imbalance.

To enable transport measurements, we fabricate two charge reservoir regions with increased interlayer spacing on the two sides of the active area. In these regions, the larger interlayer distance leads to a higher interlayer voltage difference under the same vertical electric field, creating a heavily doped electron-hole plasma (EHP) that serves as efficient exciton contacts[3,4]. Each reservoir region is equipped with one graphite contact to the $MoSe_2$ layer, and three platinum (Pt) electrodes for the WSe_2 layer. Fig. 1b shows the optical image of a representative device D1 that has a 2.3 nm (7-layer) hBN tunneling barrier. We focus on this device in the main text, but similar results are obtained in devices D2 and D3 (Extended Data Figs. 1-2). Unless otherwise noted, all measurements are performed at a lattice temperature $T = 0.01$ K.

We first characterize the device at zero magnetic field. Taking advantage of the sensitive doping dependence of optical absorption in monolayer TMDs, the charge doping phase diagram of the e-h bilayer can be determined using optical spectroscopy[3]. Fig. 1c-d shows the experimentally determined hole and electron densities n_h and n_e as functions of V_{G} and V_{B}. The constant vertical electric field $\sim 0.45\ \mathrm{V/nm}$ reduces the type-II bandgap from 1.5 eV to ~0.37 eV. The interlayer bias V_{B} controls the exciton chemical potential, and hence the effective charge gap $E_{\mathrm{g}} = 0.37\ \mathrm{eV} - V_{\mathrm{B}}$. For $V_{\mathrm{B}} < 0.34\ \mathrm{V}$, the system is a normal insulator (NI) with a finite band gap in which V_{G} can tune the system from intrinsic to either electron doped or hole doped. With a larger V_{B} ($0.34 - 0.37$ V), the charge gap becomes smaller than the interlayer exciton binding energy E_{b} but remains non-zero. The e-h bilayer is known to host an EI state at charge neutrality, which is exciton-compressible but charge-incompressible[3,4,14,15]. Increasing V_{B} further destroys the EI through an interaction-driven exciton Mott transition into an EHP phase[3,4,14].

We employ two types of transport measurements to probe exciton behavior. The first is a two-terminal resistance measurement of the WSe_2 layer, with the electron layer open-circuited (Fig. 1e). Two separate pairs of Pt electrodes are used for current sourcing and voltage sensing to eliminate the Pt-WSe_2 junction resistance (Methods). Each highly doped reservoir region acts as one terminal for the active region. The measured hole-layer resistance R_h is provided in Fig. 1f. As expected, R_h shares a similar overall shape with the n_h plot in Fig. 1c, being very resistive when $n_h = 0$. It quickly drops to kiloohm level when holes are present, with the exception of the EI phase, where it remains very resistive despite finite n_h. This is because in the EI all the holes spontaneously pair with the electrons into charge-neutral exciton, leaving no unpaired mobile charge.

The second measurement is the closed-circuit Coulomb drag experiment (Fig. 1g), where a drive current I_{drive} is passed through the $MoSe_2$ layer, and the drag current in the WSe_2 layer I_{drag} is measured. When all electrons and holes pair into excitons, their motion becomes locked, leading to perfect Coulomb drag behavior. The drag ratio in Fig. 1h, defined as $I_{\mathrm{drag}}/I_{\mathrm{drive}}$, reaches unity in the EI phase (see Extended Data Fig. 3 for raw currents). The large R_h and perfect drag are both unambiguous evidence of the EI phase.

Electron-hole fluids in a strong magnetic field

We next examine the behavior of the e-h bilayer under a strong perpendicular magnetic field B. Fig. 2a-b shows the hole resistance and drag ratio at $B = 12$ T. Compared to the zero-field case, the most noticeable difference is the emergence of quasi-periodic structures as the density varies. In the general hole-doped region, R_h exhibits pronounced QOs. Fig. 2c presents a vertical linecut of R_h at $V_{\mathrm{G}} = 0.1\ \mathrm{V}$ (blue dashed line in Fig. 2a), revealing accurately quantized plateaus at h/Ne^2 (N denotes an integer; h and e are the Planck constant and the elementary charge respectively). Meanwhile, there is negligible drag signal. This behavior is consistent with a typical 2DHG in the integer quantum Hall (QH) regime[41], where the two-terminal resistance is quantized to the Hall resistance. We assign the quantized plateaus as integer filling of hole Landau levels (LLs) $\nu_h = 1, 2, \ldots, 6$, as labeled in Fig. 2a-b. Measuring the longitudinal resistance R_{xx} and the Hall resistance R_{xy} separately confirms periodically vanishing R_{xx} and quantized R_{xy} (Extended Data Fig. 2). Apparently, metallic 2DHG transport is only weakly influenced by the electrons in the adjacent layer.

Although the interlayer coupling effects seem weak for the general $n_e \neq n_h$ case, the behavior near net charge neutrality $n_e = n_h$ displays strikingly different features. The triangular EI region in Fig. 1f and 1h evolves into a series of lobes centered along the charge neutral line (CNL, black dotted line in Fig. 2b). These lobes are characterized by increased R_h and strong drag signals. Neighboring lobes are connected at low V_{B} but become separated at higher pair densities. Within each lobe, the drag effect is strongest along the central CNL and decreases with finite e-h imbalance, eventually vanishing. Fig. 2d shows a linecut of R_h and drag ratio approximately tracing constant hole filling factor $\nu_h = 3$ (magenta dashed line in Fig. 2a). An insulating peak in R_h and a large drag ratio are observed in the charge neutral region. Away from charge neutrality, the drag signal quickly diminishes while R_h returns to its quantized value $h/3e^2$, indicating a robust hole QH state disrupted only when electron and hole densities match.

We now focus on the behaviors along the CNL. Fig. 2e displays the CNL linecut of the drag ratio and R_h. With increasing V_{B}, the drag ratio starts from a plateau at unity, followed by multiple dips at integer fillings, which deepen progressively until exciton binding is lost at $V_{\mathrm{B}} > 0.46$ V. For small integer filling factors ($\nu = 1 - 4$), the drag signal does not completely vanish at the dips, and R_h deviates from the quantized value. Both indicate LL mixing caused by strong e-h attraction. At the $\nu = 5$ dip, the drag ratio drops to zero while $R_h = h/5e^2$ becomes quantized, suggesting complete exciton destruction where electrons and holes form independent QHIs. Between adjacent QHI phases, strong exciton drag appears at partial LL fillings, with peaks near half-integer fillings. The drag current in partially filled LLs is smaller than but comparable to the drive current. A drag ratio below unity can be explained by the edge channels competing with bulk exciton transport. In addition to exciton flow, currents in both layers can also circulates through edge channels due to finite WSe_2 contact resistances (~2.4 kΩ; Extended Data Fig. 4).

The QOs and phase transitions can be understood most easily in the strong field limit in which LL mixing is weak. This applies at high densities ($V_{\mathrm{B}} > 0.4$ V), where exciton binding is weakened by many-body effects (Extended Data Fig. 5). In this regime, the electron/hole cyclotron energy $\hbar\omega_{\mathrm{c}}$ exceeds E_{b}. One can always tune V_{B} to make the energy gap between the active electron and hole LLs larger or smaller than E_{b}. As illustrated in Fig. 2f, when the LL gap exceeds E_{b}, exciton binding is destroyed, resulting in two decoupled QHIs at integer fillings. The e-h fluids form single-Slater-determinant states in which all LLs are either full or empty, and the excitonic order vanishes. Conversely, as V_{B} tunes the LL gap to be smaller than E_{b} (Fig. 2g), excitons are energetically favorable and spontaneously form. At half-filling, the ground state is known exactly in the limit of small e-h separation and has excitonic order[42]. The physics at strong magnetic fields mirrors the QH excitons previously observed in QH bilayers made of two electron layers[7,16–18], except that a net charge of zero here gives no quantized Hall resistance. At lower pair densities, where $E_{\mathrm{b}} > \hbar\omega_{\mathrm{c}}$, excitons always form regardless of e-h LL alignment. In this regime LL gap oscillations cannot fully destroy the EI, but will create a periodic modulation of drag ratio and R_h within the EI phase.

In the strong field limit, theory also predicts EI states when the electron and hole filling factors ν_e, ν_h differ by non-zero integers[25]. However, our experiments reveal clear EI signatures only near the CNL. Away from it, drag signals drop below 10%. Previous studies suggest that exciton pairing can be sensitive to the spatial structure of the two interacting LLs, favoring those with similar spatial wavefunctions[43]. In our density range ($\nu \leq 6$), both $MoSe_2$ electron and WSe_2 hole LLs are fully valley-polarized[44,45]. The CNL is unique because the electron and hole LLs share the same orbital index. This may explain the lack of excitonic features for $\nu_e \neq \nu_h$, as they may require substantially stronger field, cleaner samples, and/or lower temperature. A full understanding of imbalanced e-h fluids will require further investigation.

Fan diagram at net charge neutrality

In the strong field limit, e-h bilayers and previously studied electron-electron bilayers should have identical bulk properties. However, at weaker fields, excitonic order rapidly decays in electron-electron systems, but persists in e-h systems. Fig. 3a shows the B dependence of the drag ratio along the CNL. The NI, EI and EHP phases have distinct drag characteristics. In the NI phase at low V_{B}, the single-particle gap remains stable against magnetic fields – no drive or drag current is detected at any B. At intermediate V_{B}, the EI phase yields large drag ratios. With increasing magnetic field, the EI region extends to higher V_{B} due to increased exciton binding energy[46]. Within the EI, QOs emerge when $B \gtrsim 5$ T, forming Landau-fan-like patterns. In the high-density EHP phase, a weak frictional drag oscillates with B. Corresponding behaviors also appear in the R_h data in Fig. 3b: the NI phase remains resistive, the resistance in the EI phase forms Landau-fan-like structures aligned with drag signals, and the EHP phase develops QH resistance plateaus at high field.

Fig. 3c shows three linecuts of R_h and drag ratio at fixed V_{B} values, plotted against $1/B$. They represent different regimes in the EI phase regarding the relative strength between E_{b} and $\hbar\omega_{\mathrm{c}}$. The cyclotron energy scales with B, reaching ~3 meV at 12 T. The exciton binding energy starts near 20 meV at low density and decreases at higher V_{B} (Extended Data Fig. 5). At $V_{\mathrm{B}} = 0.35$ V (upper panel), where $E_{\mathrm{b}} \gg \hbar\omega_{\mathrm{c}}$, R_h remains above our 1 MΩ measurement range regardless of B, and the drag ratio remains unity with no noticeable QOs. For $V_{\mathrm{B}} = 0.41$ V (middle panel) the reduced E_{b} becomes comparable to $\hbar\omega_{\mathrm{c}}$. Clear QOs appear in both drag ratio and R_h, which are periodic in $1/B$. When $E_{\mathrm{b}} < \hbar\omega_{\mathrm{c}}$ at $V_{\mathrm{B}} = 0.43$ V, larger oscillations touch zero at integer LL filling, indicating reentrant EI-QHI transitions in the quantized regime.

The magnetic oscillations in EIs have the same $1/B$ periodicity as conventional magnetic oscillations in metallic states[47] because both reflect oscillations with period one in LL filling factor, although the mechanism in EIs differs from either Shubnikov-de Haas or de Haas-van Alphen effects. Because QH states are most favored each time the electron and hole filling factors $\frac{nh}{eB}$ become an integer, the $1/B$ periodicity is

216 $$\Delta\left(\frac{1}{B}\right) = \frac{e}{nh}.$$

The experimentally extracted period agrees with the optically measured carrier densities (Extended Data Fig. 6), supporting our interpretation. In our device geometry the carrier densities in graphite gates are always much higher than n_e and n_h (Extended Data Fig. 7) , ruling out the possibility that the observed QOs arise from gate-induced potential modulations[48], which would produce a very different frequency.

Our observation of excitonic QOs and EI-QHI transitions agrees qualitatively with the theoretical predictions[24,25]. The experimentally observed critical magnetic field, however, is much lower.

While gate screening and sample disorder may partly account for this discrepancy, we believe that substantial differences would remain even in ideal conditions. This is likely because of the well-known tendency for mean-field theory to overestimate the robustness of ordered states, particularly in the high-density regime where many-body interactions become important. Improving quantitative agreement between theory and experiment stands as an important challenge.

Finite-temperature phase diagram

Finally, we explore the phase diagram as a function of the pair density and temperature. Fig. 4a shows the temperature dependence of the drag ratio at $B = 12$ T along the CNL. Multiple EI domes emerge at low temperatures, roughly centered around half-integer fillings up to filling factor 6. With increased temperature, the drag ratio sharply drops to zero for high-order EI domes, while lower-order ones show smoother transitions (Fig. 4b). The lower exciton melting temperatures at larger filling factors are consistent with reduced binding energy when both electrons and holes are limited to high LLs. The corresponding R_h (Fig. 4c-d) decreases with temperature, confirming the insulating nature of these EI phases.

Although the QO amplitude decreases monotonically with temperature, it follows two distinct scaling behaviors between the low-temperature EI phase and high-temperature QH liquid phase. In the QH liquid, resistance oscillations in WSe_2 follow the Lifshitz–Kosevich (LK) formula with an effective hole mass of ~$0.5m_0$ (where m_0 denotes the bare electron mass), similar to the behavior of QOs in metallic 2D hole liquids (Extended Data Fig. 8). In contrast, in the low-temperature EI regime the resistance deviates from LK scaling, which is governed by thermal activation of excitons instead. With increasing temperature, more excitons are thermally ionized into highly mobile charges, which reduces the QO amplitude.

Interestingly, we observe temperature-induced EI-QHI phase transitions at small integer filling factors. As seen in Fig. 4a and Fig. 2e, the drag ratio dips at $\nu = 1 - 4$ does not reach zero at our lowest temperature due to finite LL mixing from Coulomb interactions. Fig. 4e-f shows the temperature dependence of R_h and the drag ratio at $\nu = 3$ and 4. The drag ratio rapidly decreases beyond ~5 K for $\nu = 3$ and ~2 K for $\nu = 4$. Meanwhile, the deviations of R_h from $h/\nu e^2$ also disappear, recovering the quantized values in the QHI. These observations suggest temperature-driven phase transitions, where thermal energy melts the excitons in the EI and restores the QHI phase.

In summary, we have studied the transport behavior of e-h fluids under magnetic fields and uncovered a rich phase diagram featuring excitonic QOs and reentrant EI-QHI phase transitions. The presence of QOs in our insulating system highlights unconventional insulating phases beyond single-particle band theory. Although QOs in narrow-gap insulators have been reported[37–40], their physical origins remain debated in most prior systems[26–36,48]. With full gate control across different doping phases, optical determination of particle densities in each layer, and separate electrical access to electrons and holes, we conclusively attribute the observed QOs to the EI state, confirming theoretical predictions. These findings establish TMD-based e-h bilayers as a promising platform for further exploration of exciton physics, such as exciton superfluids, vortex lattices[49], and fractional exciton states.

Acknowledgements

This work was primarily funded by the U.S. Department of Energy, Office of Science, Basic Energy Sciences, Materials Sciences and Engineering Division under Contract No. DE-AC02-05-CH11231 within the van der Waals heterostructure program KCFW16 (device fabrication and transport measurements). Optical characterization was supported by the AFOSR award FA9550-23-1-0246. K.W. and T.T. acknowledge support from the Japan Society for the Promotion of Science (KAKENHI grants 21H05233 and 23H02052) and World Premier International Research Center Initiative, Ministry of Education, Culture, Sports, Science and Technology, Japan. R.Q. acknowledges support from Kavli ENSI graduate student fellowship.

Author contributions

F.W. and R.Q. conceived the research. Q.L, R.Q. and J.N. fabricated the devices with help from Z.C and S.C. R.Q. performed the optical measurements. R.Q. and Z.Z. performed the transport measurements with help from H.K., J.X. and C.S. R.Q., Z.Z. and F.W. analyzed the data with inputs from M.F.C., B.Z. and A.H.M. K.W. and T.T. grew hBN crystals. All authors discussed the results and wrote the manuscript.

Competing interests

The authors declare no competing interests.

Figures

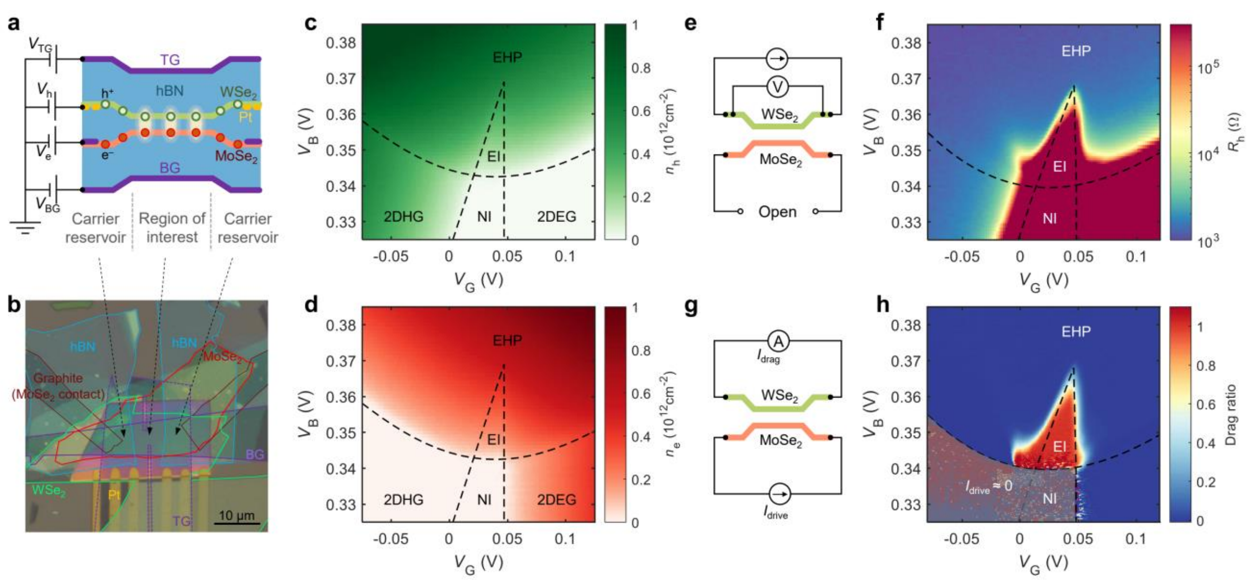

Fig. 1 | Strongly coupled electron-hole bilayers.

a, Schematic cross-section of the electron-hole bilayer device based on the $MoSe_2$/hBN/WSe_2 heterostructure. **b**, An optical microscopy image of device D1 (WSe_2/7-layer hBN/$MoSe_2$ heterostructure), with flake boundaries outlined. **c-d**, Experimentally determined hole density n_h in the WSe_2 layer (**c**) and electron density n_e in the $MoSe_2$ layer (**d**), respectively, measured at zero magnetic field and a lattice temperature $T = 0.01$ K. The phase diagram is composed of normal insulator (NI), excitonic insulator (EI), two-dimensional electron gas (2DEG), two-dimensional hole gas (2DHG), and electron-hole plasma (EHP) regions. The vertical electric field is fixed by antisymmetric gating $V_{\mathrm{BG}} - V_{\mathrm{TG}} = 7$ V. **e**, Circuit diagram of the two-terminal hole resistance measurement. The resistance in the WSe_2 layer is measured with the $MoSe_2$ layer open-circuited. **f**, Measured hole resistance R_h as a function of V_{G} and V_{B} at zero magnetic field. The EI region exhibits a large R_h despite finite n_h. **g**, Circuit diagram of the closed-circuit Coulomb drag measurement. A drive current is passed through the $MoSe_2$ layer, and the closed-circuit drag current in the WSe_2 layer is measured. **h**, Measured drag ratio $I_{\mathrm{drag}}/I_{\mathrm{drive}}$ as a function of V_{G} and V_{B} at zero magnetic field. Perfect Coulomb drag is observed in the EI region. The bottom-left region shaded with semitransparent gray color is noisy due to the absence of any drive current when $n_e = 0$.

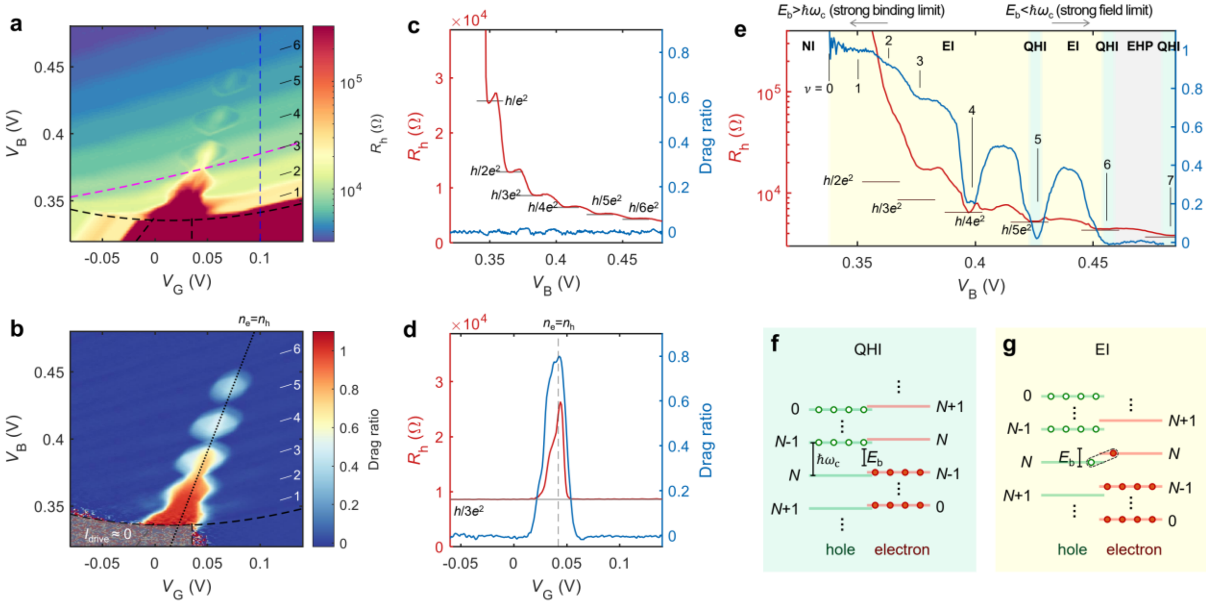

Fig. 2 | Electron-hole fluids in a strong magnetic field.

a, R_h as a function of V_{G} and V_{B} at $B = 12$ T. Landau quantization of holes leads to quasi-periodic structures following n_h contour lines outside the EI region. The EI region develops into a series of lobes centered near the CNL and exhibits increased R_h values. **b**, Closed-circuit drag ratio $I_{\mathrm{drag}}/I_{\mathrm{drive}}$ at $B = 12$ T. Strong Coulomb drag is observed in the EI region near the CNL, which matches the EI region in **a**. Other regions show negligible drag signal. **c**, V_{B} dependence of R_h (left axis) and the drag ratio (right axis) at fixed gating $V_{\mathrm{G}} = 0.10$ V (blue dashed line in **a**), where the electron and hole densities are not equal. At integer hole filling factors, R_h quantizes at h/Ne^2, indicating QH states of holes. **d**, Line cut of R_h (left axis) and the drag ratio (right axis) along fixed hole LL filling $\nu_h = 3$ (magenta dashed line in **a**). R_h deviates from $h/3e^2$ only near the net charge neutrality, accompanied by a simultaneous increase in the drag signal. **e**, Line cut of R_h (left axis) and the drag ratio (right axis) along the net CNL $n_e = n_h$ (black dotted line in **b**). Clear QOs can be observed in both R_h and drag signals. Multiple EI-QHI phase transitions happen at higher V_{B}, where the exciton binding energy and the cyclotron energy are comparable and compete with each other. The EI regions are characterized by a large drag signal and enhanced R_h, while the QHI regions exhibit quantized $R_h$values and very small drag signal. The EI, QHI, and EHP regions are highlighted with yellow, green, and grey shade, respectively. **f-g**, Schematic LL structures in the bilayer QHI phase (**f**) and the EI phase (**g**) in the strong field limit, $\hbar\omega_c > E_b$. Depending on the relative size of the LL gap and E_b, excitons can be fully destroyed (QHI phase in **f**) or spontaneously created (EI phase in **g**).

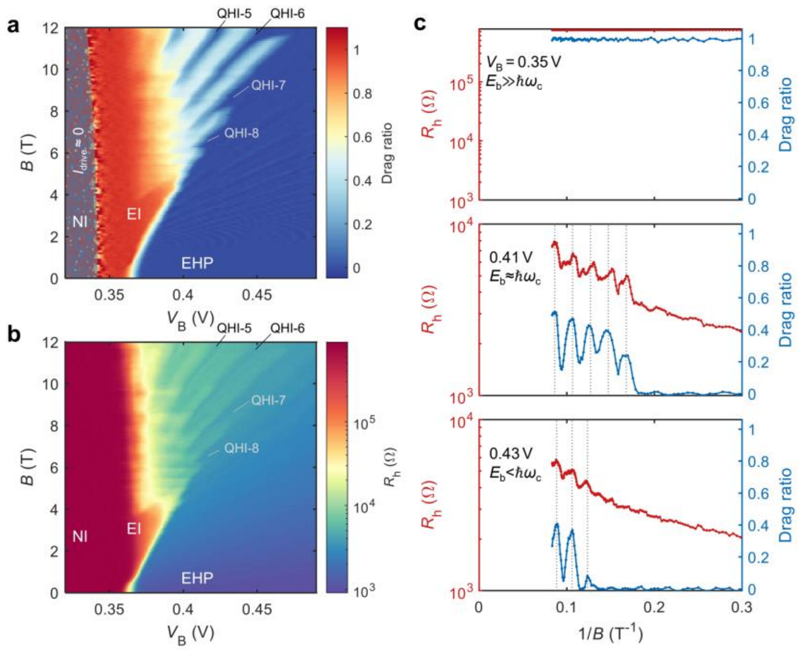

Fig. 3 | Quantum oscillations at net charge neutrality.

a, Closed-circuit drag ratio as a function of perpendicular magnetic field B and interlayer bias voltage V_B. QOs in the EI phase start to develop at $B \gtrsim 5$ T, and evolve into EI-QHI phase transitions at higher B. **b**, R_h as a function of B and V_B. The Landau-fan-like structures match with corresponding features in **a**. **c**, Magnetic field dependence of R_h (left axis) and the drag ratio (right axis) at three typical V_B values. At small V_B (top panel), no QO is observed due to the large exciton binding energy at low density. At higher V_B (middle and bottom panels), clear QOs with $1/B$ periodicity show up in both R_h and drag signals.

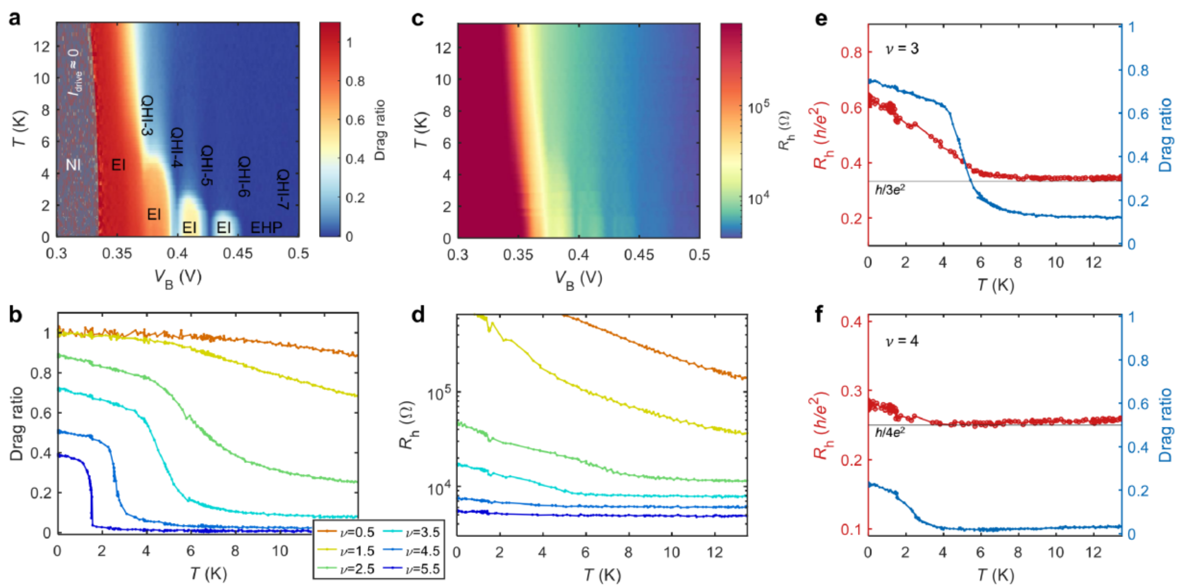

Fig. 4 | Finite temperature phase diagram at net charge neutrality.

a, Drag ratio along the CNL at $B = 12$ T for different V_B and temperatures. Multiple EI domes are centered around half-integer fillings. High-order EI regions are separated by QHI states, while the lower ones are connected. The exciton ionization temperature decreases with the exciton density (i.e. higher V_B). **b**, Linecuts of the drag ratio at different half-integer LL fillings as a function of temperature. **c**, R_h along the CNL at $B = 12$ T for different V_B and temperatures. R_h decreases with increasing temperature in the EI phases, confirming the insulating behavior. **d**, Linecuts of R_h at half-integer LL fillings as a function of temperature. **e-f**, R_h (left axis) and the drag ratio (right axis) at integer LL filling $\nu_e = \nu_h = 3$ (**e**) and 4 (**f**) as a function of temperature. The strong decrease of drag signals and the recovery of R_h quantization at elevated temperature suggests thermally driven EI-QHI phase transitions, in which thermal energy assists the cyclotron energy to dissociate exciton pairing.

References

1. Y. Zeng & A.H. MacDonald. Electrically controlled two-dimensional electron-hole fluids. *Phys. Rev. B* **102**, 085154 (2020).

2. F.-C. Wu, F. Xue & A.H. MacDonald. Theory of two-dimensional spatially indirect equilibrium exciton condensates. *Phys. Rev. B* **92**, 165121 (2015).

3. R. Qi, A.Y. Joe, Z. Zhang, Y. Zeng, T. Zheng, Q. Feng, J. Xie, E. Regan, Z. Lu, T. Taniguchi, K. Watanabe, S. Tongay, M.F. Crommie, A.H. MacDonald & F. Wang.

Thermodynamic behavior of correlated electron-hole fluids in van der Waals heterostructures. *Nat. Commun.* **14**, 8264 (2023).

4. L. Ma, P.X. Nguyen, Z. Wang, Y. Zeng, K. Watanabe, T. Taniguchi, A.H. MacDonald, K.F. Mak & J. Shan. Strongly correlated excitonic insulator in atomic double layers. *Nature* **598**, 585–589 (2021).
5. S. De Palo, F. Rapisarda & G. Senatore. Excitonic Condensation in a Symmetric Electron-Hole Bilayer. *Phys. Rev. Lett.* **88**, 206401 (2002).
6. M.M. Fogler, L.V. Butov & K.S. Novoselov. High-temperature superfluidity with indirect excitons in van der Waals heterostructures. *Nat. Commun.* **5**, 4555 (2014).
7. X. Liu, K. Watanabe, T. Taniguchi, B.I. Halperin & P. Kim. Quantum Hall drag of exciton condensate in graphene. *Nat. Phys.* **13**, 746–750 (2017).
8. J.P. Eisenstein & A.H. MacDonald. Bose–Einstein condensation of excitons in bilayer electron systems. *Nature* **432**, 691–694 (2004).
9. X. Zhu, P.B. Littlewood, M.S. Hybertsen & T.M. Rice. Exciton Condensate in Semiconductor Quantum Well Structures. *Phys. Rev. Lett.* **74**, 1633–1636 (1995).
10. R. Maezono, P. López Ríos, T. Ogawa & R.J. Needs. Excitons and biexcitons in symmetric electron-hole bilayers. *Phys. Rev. Lett.* **110**, 216407 (2013).
11. D.D. Dai & L. Fu. Strong-Coupling Phases of Trions and Excitons in Electron-Hole Bilayers at Commensurate Densities. *Phys. Rev. Lett.* **132**, 196202 (2024).
12. R. Qi, Q. Li, Z. Zhang, S. Chen, J. Xie, Y. Ou, Z. Cui, D.D. Dai, A.Y. Joe, T. Taniguchi, K. Watanabe, S. Tongay, A. Zettl, L. Fu & F. Wang. Electrically controlled interlayer trion fluid in electron-hole bilayers. Preprint at https://doi.org/10.48550/arXiv.2312.03251 (2023).

13. P.X. Nguyen, R. Chaturvedi, L. Ma, P. Knuppel, K. Watanabe, T. Taniguchi, K.F. Mak & J. Shan. A degenerate trion liquid in atomic double layers. Preprint at https://doi.org/10.48550/arXiv.2312.12571 (2023).
14. P.X. Nguyen, L. Ma, R. Chaturvedi, K. Watanabe, T. Taniguchi, J. Shan & K.F. Mak. Perfect Coulomb drag in a dipolar excitonic insulator. *Science* **388**, 274–278 (2025).
15. R. Qi, A.Y. Joe, Z. Zhang, J. Xie, Q. Feng, Z. Lu, Z. Wang, T. Taniguchi, K. Watanabe, S. Tongay & F. Wang. Perfect Coulomb drag and exciton transport in an excitonic insulator. *Science* **388**, 278–283 (2025).
16. X. Liu, J.I.A. Li, K. Watanabe, T. Taniguchi, J. Hone, B.I. Halperin, P. Kim & C.R. Dean. Crossover between strongly coupled and weakly coupled exciton superfluids. *Science* **375**, 205–209 (2022).
17. J.P. Eisenstein. Exciton Condensation in Bilayer Quantum Hall Systems. *Annu. Rev. Condens. Matter Phys.* **5**, 159–181 (2014).
18. J.I.A. Li, T. Taniguchi, K. Watanabe, J. Hone & C.R. Dean. Excitonic superfluid phase in double bilayer graphene. *Nat. Phys.* **13**, 751–755 (2017).
19. A.F. Croxall, K. Das Gupta, C.A. Nicoll, M. Thangaraj, H.E. Beere, I. Farrer, D.A. Ritchie & M. Pepper. Anomalous Coulomb Drag in Electron-Hole Bilayers. *Phys. Rev. Lett.* **101**, 246801 (2008).
20. L. Du, X. Li, W. Lou, G. Sullivan, K. Chang, J. Kono & R.-R. Du. Evidence for a topological excitonic insulator in InAs/GaSb bilayers. *Nat. Commun.* **8**, 1971 (2017).
21. R. Wang, T.A. Sedrakyan, B. Wang, L. Du & R.-R. Du. Excitonic topological order in imbalanced electron–hole bilayers. *Nature* **619**, 57–62 (2023).

22. Z. Han, T. Li, L. Zhang, G. Sullivan & R.-R. Du. Anomalous Conductance Oscillations in the Hybridization Gap of InAs/GaSb Quantum Wells. *Phys. Rev. Lett.* **123**, 126803 (2019).
23. D. Xiao, C.-X. Liu, N. Samarth & L.-H. Hu. Anomalous Quantum Oscillations of Interacting Electron-Hole Gases in Inverted Type-II InAs/GaSb Quantum Wells. *Phys. Rev. Lett.* **122**, 186802 (2019).
24. Y. Shao & X. Dai. Quantum oscillations in an excitonic insulating electron-hole bilayer. *Phys. Rev. B* **109**, 155107 (2024).
25. B. Zou, Y. Zeng, A.H. MacDonald & A. Strashko. Electrical control of two-dimensional electron-hole fluids in the quantum Hall regime. *Phys. Rev. B* **109**, 085416 (2024).
26. L. Li, K. Sun, C. Kurdak & J.W. Allen. Emergent mystery in the Kondo insulator samarium hexaboride. *Nat. Rev. Phys.* **2**, 463–479 (2020).
27. H. Pirie, E. Mascot, C.E. Matt, Y. Liu, P. Chen, M.H. Hamidian, S. Saha, X. Wang, J. Paglione, G. Luke, D. Goldhaber-Gordon, C.F. Hirjibehedin, J.C.S. Davis, D.K. Morr & J.E. Hoffman. Visualizing the atomic-scale origin of metallic behavior in Kondo insulators. *Science* **379**, 1214–1218 (2023).
28. H. Shen & L. Fu. Quantum Oscillation from In-Gap States and a Non-Hermitian Landau Level Problem. *Phys. Rev. Lett.* **121**, 026403 (2018).
29. L. Zhang, X.-Y. Song & F. Wang. Quantum Oscillation in Narrow-Gap Topological Insulators. *Phys. Rev. Lett.* **116**, 046404 (2016).
30. J. Knolle & N.R. Cooper. Quantum Oscillations without a Fermi Surface and the Anomalous de Haas-van Alphen Effect. *Phys. Rev. Lett.* **115**, 146401 (2015).
31. J. Knolle & N.R. Cooper. Excitons in topological Kondo insulators: Theory of thermodynamic and transport anomalies in SmB6. *Phys. Rev. Lett.* **118**, 096604 (2017).

32. O. Erten, P.-Y. Chang, P. Coleman & A.M. Tsvelik. Skyrme Insulators: Insulators at the Brink of Superconductivity. *Phys. Rev. Lett.* **119**, 057603 (2017).

33. P.A. Lee. Quantum oscillations in the activated conductivity in excitonic insulators: Possible application to monolayer WTe2. *Phys. Rev. B* **103**, L041101 (2021).

34. W.-Y. He & P.A. Lee. Quantum oscillation of thermally activated conductivity in a monolayer WTe2-like excitonic insulator. *Phys. Rev. B* **104**, L041110 (2021).

35. D. Chowdhury, I. Sodemann & T. Senthil. Mixed-valence insulators with neutral Fermi surfaces. *Nat. Commun.* **9**, 1766 (2018).

36. I. Sodemann, D. Chowdhury & T. Senthil. Quantum oscillations in insulators with neutral Fermi surfaces. *Phys. Rev. B* **97**, 045152 (2018).

37. G. Li, Z. Xiang, F. Yu, T. Asaba, B. Lawson, P. Cai, C. Tinsman, A. Berkley, S. Wolgast, Y.S. Eo, D.-J. Kim, C. Kurdak, J.W. Allen, K. Sun, X.H. Chen, Y.Y. Wang, Z. Fisk & L. Li. Two-dimensional Fermi surfaces in Kondo insulator SmB6. *Science* **346**, 1208–1212 (2014).

38. B.S. Tan, Y.-T. Hsu, B. Zeng, M.C. Hatnean, N. Harrison, Z. Zhu, M. Hartstein, M. Kiourlappou, A. Srivastava, M.D. Johannes, T.P. Murphy, J.-H. Park, L. Balicas, G.G. Lonzarich, G. Balakrishnan & S.E. Sebastian. Unconventional Fermi surface in an insulating state. *Science* **349**, 287–290 (2015).

39. P. Wang, G. Yu, Y. Jia, M. Onyszczak, F.A. Cevallos, S. Lei, S. Klemenz, K. Watanabe, T. Taniguchi, R.J. Cava, L.M. Schoop & S. Wu. Landau quantization and highly mobile fermions in an insulator. *Nature* **589**, 225–229 (2021).

40. Z. Xiang, Y. Kasahara, T. Asaba, B. Lawson, C. Tinsman, L. Chen, K. Sugimoto, S. Kawaguchi, Y. Sato, G. Li, S. Yao, Y.L. Chen, F. Iga, J. Singleton, Y. Matsuda & L. Li. Quantum oscillations of electrical resistivity in an insulator. *Science* **362**, 65–69 (2018).

41. G.L.J.A. Rikken, J.A.M.M. van Haaren, W. van der Wel, A.P. van Gelder, H. van Kempen, P. Wyder, J.P. André, K. Ploog & G. Weimann. Two-terminal resistance of quantum Hall devices. *Phys. Rev. B* **37**, 6181–6186 (1988).

42. K. Moon, H. Mori, K. Yang, S.M. Girvin, A.H. MacDonald, L. Zheng, D. Yoshioka & S.-C. Zhang. Spontaneous interlayer coherence in double-layer quantum Hall systems: Charged vortices and Kosterlitz-Thouless phase transitions. *Phys. Rev. B* **51**, 5138–5170 (1995).

43. T. Jungwirth, S.P. Shukla, L. Smrčka, M. Shayegan & A.H. MacDonald. Magnetic Anisotropy in Quantum Hall Ferromagnets. *Phys. Rev. Lett.* **81**, 2328–2331 (1998).

44. Q. Shi, E.-M. Shih, M.V. Gustafsson, D.A. Rhodes, B. Kim, K. Watanabe, T. Taniguchi, Z. Papić, J. Hone & C.R. Dean. Odd- and even-denominator fractional quantum Hall states in monolayer WSe2. *Nat. Nanotechnol.* **15**, 569–573 (2020).

45. S. Larentis, H.C.P. Movva, B. Fallahazad, K. Kim, A. Behroozi, T. Taniguchi, K. Watanabe, S.K. Banerjee & E. Tutuc. Large effective mass and interaction-enhanced Zeeman splitting of K -valley electrons in MoSe 2. *Phys. Rev. B* **97**, 201407 (2018).

46. E.W. Fenton. Excitonic Insulator in a Magnetic Field. *Phys. Rev.* **170**, 816–821 (1968).

47. D. Shoenberg. *Magnetic Oscillations in Metals*. (Cambridge University Press, 2009).

48. J. Zhu, T. Li, A.F. Young, J. Shan & K.F. Mak. Quantum Oscillations in Two-Dimensional Insulators Induced by Graphite Gates. *Phys. Rev. Lett.* **127**, 247702 (2021).

49. B. Zou & A.H. MacDonald. Vortex lattice states of bilayer electron-hole fluids in quantizing magnetic fields. Preprint at https://doi.org/10.48550/arXiv.2411.08810 (2024).

Methods

Device fabrication. We use a dry-transfer method based on polyethylene terephthalate glycol (PETG) stamps to fabricate the heterostructures. Monolayer $MoSe_2$, monolayer WSe_2, few-layer graphene and hBN flakes are mechanically exfoliated from bulk crystals onto SiO_2/Si substrates. We use 6-10 nm hBN as the gate dielectric and 2-3 nm thin hBN as the interlayer spacer. Prior to the stacking process, metal electrodes for the hole layer (7 nm Pt with 3 nm Cr adhesion layer) are defined using photolithography (Durham Magneto Optics, MicroWriter) and electron beam evaporation (Angstrom Engineering) onto a high resistivity SiO_2/Si substrate. The graphite top gate is cut using an atomic force microscope tip[50] to eliminate undesired current paths in the unmatched WSe_2 monolayer regions.

A 0.5 mm thick clear PETG stamp is employed to pick up the flakes at 65-75 °C. A >100 nm thick hBN is first picked up by the stamp to protect the following layers. Then the graphite top gate, the top dielectric hBN, the monolayer WSe_2, the thin hBN spacer, the two thicker hBN spacers in the reservoir regions, the two graphite contacts, the monolayer $MoSe_2$, the bottom dielectric hBN, and the bottom graphite gate are sequentially picked up. The whole stack is released onto the prepatterned Pt electrodes at 100 °C, followed by dissolving the PETG in chloroform for one day. Finally, metal electrodes (5 nm Cr/60 nm Au) are defined using photolithography and electron beam evaporation.

Optical measurements. All the optical and transport measurements are performed in a dilution refrigerator (Bluefors LD250) with a base lattice temperature of 10 mK. The signal wires are filtered at the mixing chamber flange (QDevil) before reaching the sample. The d.c. voltages on the device are applied with Keithley 2400/2450 source meters or Keithley 2502 picoammeters. The reflection spectroscopy is performed with a supercontinuum laser (YSL Photonics) as the light source. The laser is focused on the sample by a 10× objective (Olympus PLN 10X). The reflected light is collected after a spectrometer by a CCD camera (Andor Shamrock 303i) with 1000 ms exposure time. We use reflection spectroscopy to determine the electron and hole densities shown in Fig. 1c-d and Extended Data Figs. 5-6. A detailed description of the methodology can be found in ref.[3].

WSe_2 hole resistance measurements. The detailed circuit diagram for the two-terminal WSe_2 hole resistance measurements is shown in Extended Data Fig. 9a. Good electrical contacts are crucial for accurate two-terminal resistance measurements of QH devices. In our device geometry, the contact resistance includes two parts: the resistance at Pt to WSe_2 junction, and resistance at the reservoir region to region of interest junction. Since we have multiple Pt electrodes in each reservoir region, we exclude the Pt-WSe_2 junction resistance using two separate pairs of Pt electrode for sourcing the current and measuring the voltage. A current excitation at 17 Hz is applied between two WSe_2 electrodes, and the voltage drop between another two electrodes is used to determine the hole layer resistance. However, note that multiple contacts are connected to the same highly doped reservoir region. It does not exclude the contact resistance from the reservoirs to the region of interest. Therefore, the measured R_h should be interpreted as two-terminal resistance in the QH regime[41], where each highly doped reservoir region acts as one terminal.

The Pt-WSe_2 contact resistance can be determined by comparing the resistance using two different measurement configurations shown in Extended Data Fig. 4a. In configuration I, all three Pt electrodes in each reservoir region are linked together to source currents and measure the voltage drop. The resulting two-terminal resistance includes the Pt-WSe_2 contact resistance. In configuration II (the configuration used in the main text), different pairs of Pt electrodes are used for current excitation and voltage measurement, excluding the Pt-WSe_2 contact resistance.

Extended Data Fig. 4b shows the measured resistance of the two configurations. Their difference is around 2 kΩ and depends weakly on the magnetic field.

Coulomb drag measurements. Extended Data Fig. 9b shows the detailed circuit diagram of the Coulomb drag measurements. Closed-circuit drag measurements require good electrical contacts for the drag layer. The graphite-$MoSe_2$ contact resistance is 2-3 MΩ, much larger than the Pt-WSe_2 contact. We therefore choose the $MoSe_2$ layer as the drive layer and the WSe_2 layer as the drag layer. A 5 mV_{rms} a.c. voltage excitation at 17 Hz is applied between the two $MoSe_2$ contacts. A 10 kΩ potentiometer is used to distribute the a.c. voltage between the two contacts to minimize interlayer capacitive coupling. The drag current is measured between the left three WSe_2 electrodes and the right three WSe_2 electrodes.

The interlayer tunnelling current is at picoampere level (Extended Data Fig. 10), providing a lower bound of the tunnelling resistance $> 10^{10}$ Ω. This is many orders of magnitude larger than the in-plane resistance, and therefore its contribution to the measured drive and drag currents is negligible.

Data availability

All data that support the findings of this study are available from the corresponding author upon request. Source data are provided with this paper.

Methods-only References

50. H. Li, Z. Ying, B. Lyu, A. Deng, L. Wang, T. Taniguchi, K. Watanabe & Z. Shi. Electrode-Free Anodic Oxidation Nanolithography of Low-Dimensional Materials. *Nano Lett.* **18**, 8011–8015 (2018).